Applied Geochemistry 150 (2023) 105589

Contents lists available at ScienceDirect

Applied Geochemistry

journal homepage: www.elsevier.com/locate/apgeochem

Exploring the role of the structural heterogeneity of fractured carbonate reservoirs in contact with dissolved CO_2 based on fracture-water-rock simulation experiments

Qian Ding [a,b,c], Jingbin Wang [a,b,c], Leilei Yang [d,e], Dongya Zhu [a,b,c], Wenbin Jiang [f,g], Zhiliang He [a,c,h,*]

[a] State Key Laboratory of Shale Oil and Gas Accumulation Mechanism and the Effective Development, Beijing, 102206, China
[b] Petroleum Exploration and Production Research Institute, SINOPEC, Beijing, 102206, China
[c] Key Laboratory of Geology and Resource in Deep Stratum, SINOPEC, Beijing, 102206, China
[d] State Key Laboratory of Petroleum Resource and Prospecting, Beijing, 102249, China
[e] China University of Petroleum, Beijing, 102249, China
[f] Institute of Mechanics, Chinese Academy of Sciences, Beijing, 100190, China
[g] School of Engineering Science, University of Chinese Academy of Sciences, Beijing, 100190, China
[h] China Petroleum & Chemical Corporation, Beijing, 100728, China

ARTICLE INFO

Editorial handling by Liwei Zhang

Keywords:
Brine with dissolved CO_2
Dissolution pattern
Structural heterogeneity
Fractured limestone
Tarim basin

ABSTRACT

Based on the geological background of ultra-deep fractured carbonate reservoirs in the Shunbei oil and gas field, the objective of this study was to clarify the interactions between fractured carbonate reservoirs and formation fluids (brine with dissolved CO_2) under deep strata, and the potential impact of these interactions on reservoirs. In this study, high-temperature and high-pressure simulation experiments and numerical simulations based on the Yijianfang Formation in the Shunbei area were designed to investigate the influence of temperature, pressure, fluid, and structural heterogeneity on fluid transport and mass transfer, calculate the ion diffusion characteristics and the trend of mineral dissolution/precipitation along the fractures, and clarify the change in the reservoir space. The results indicated that the volume of the main fracture increased after the reaction between an acidic solution and a formation sample, the permeability of the sample increased by orders of magnitude, and its porosity increased accordingly. The overall reaction during the experimental period was dominated by the dissolution of calcium carbonate, and no calcium carbonate precipitated. The structural heterogeneity and hydraulic properties of the sample make the main flow channel a main fracture. The flow and reaction processes in the flow channel promoted each other. The effects of temperature and pressure on the overall reservoir space were insignificant. Branch fractures or microfractures can weaken the main fluid flow rate and tend to result in the accumulation of solutes, the ends of which may be potential locations for mineral precipitation. Therefore, the priority exploration location for deep and ultra-deep fractured reservoirs should be the main fractures upstream of the fluid flow.

1. Introduction

Deep and ultra-deep marine carbonates are rich in hydrocarbon resources and are natural areas for China's energy succession (He et al., 2017a,b; Ma et al., 2020, 2022). A breakthrough was made in exploring ultra-deep ancient carbonate strata in the Shunbei region of the Tarim Basin in China. The main target layer of the Shunbei oil and gas field is the Ordovician Yingshan Formation - Yijianfang Formation, with a burial depth of 7200–8,000 m. Shunbei, an oil and gas field, submitted cumulative proven reserves of 2×10^8 t (oil equivalent) by the end of 2021 (Qi, 2020, 2021; Deng and Spycher, 2019; 2022; Ma et al., 2022). The reservoir space of the Shunbei oil and gas field is a system of fractures and cavities formed by tectonic activities with strong spatial heterogeneity (Qi, 2020; Ma et al., 2020, 2022). Structural fault and fluid activities play a vital role in controlling the formation and distribution of carbonate reservoirs (Han et al., 2016; Lu et al., 2017; He et al., 2017a,

* Corresponding author. State Key Laboratory of Shale Oil and Gas Accumulation Mechanism and the Effective Development, Beijing, 102206, China.
E-mail address: hezhiliang@sinopec.com (Z. He).

https://doi.org/10.1016/j.apgeochem.2023.105589
Received 4 August 2022; Received in revised form 16 January 2023; Accepted 30 January 2023
Available online 2 February 2023

b). Different types of geological fluids flow along the fractures, react with the surrounding rock, dissolve or precipitate minerals, change the pore space geometry, and affect fluid flow paths and solute transport. (Davies and Smith, 2006; Luquot and Gouze, 2009; Chen et al., 2014; Garcia-Rios et al., 2017). One of the aims of our study was to qualitatively and quantitatively clarify the influence of structural heterogeneity and fluid-rock interaction in the fracture-fluid-rock system to clarify the genesis mechanism of deep and ultra-deep fractured carbonate reservoirs and provide a theoretical and predictive basis for the reservoir of the Shunbei oil and gas fields.

Predicting mass transfer and fluid flow in fractured rocks, couples physical flow processes and chemical reaction processes, is still a challenge because the heterogeneity of the fractures and chemical reaction processes are complex. For fluid-rock systems, laboratory-scale experiments are generally used to simulate the reaction process, and numerical simulations are used to study the fluid-mineral reaction mechanism at the pore scale. Laboratory-scale experiments identify fluid-rock interactions through equipment such as mixed-flow reactors, rotating disks, and high-temperature and high-pressure reactors. Core flooding testing is a useful experimental method for investigating the coupled flow and reaction processes in a rock matrix. During such tests, reactions in the fluid-rock system are studied by sampling and analyzing the effluent. Inductively coupled plasma-mass spectroscopy, ion chromatography analysis, and pH probes have often been used to measure the concentrations of the chemical species of interest in effluent samples (Noiriel et al., 2005, 2009; Smith et al., 2013, 2014, 2017; Al-Khulaifi et al., 2018). Scanning electron microscopy (SEM), atomic force microscopy (AFM), and X-ray computed microtomography (XCMT) scans were performed on the specimens before and after experiments to study changes in the mineral dissolution-precipitation interface and pore space (Gouze et al., 2003; Noiriel et al., 2004, 2018, 2021; Deng et al., 2015, 2017; Noiriel, 2015; Noiriel and Deng, 2018). These experimental studies have provided a good understanding of the factors that influence rock matrix dissolution (Li et al., 2019a). The water-rock ratio, temperature and pressure, lithology, mineral distribution, particle diameter, pore connectivity, pore geometry, surface roughness, and physicochemical conditions of the fluid combine to control the reaction process of the fluid-rock system (Wellman et al., 2003; Steefel et al., 2005; Brantley, 2008; Luquot and Gouze, 2009; Chen et al., 2014; Noiriel, 2015; 2017; He et al., 2017a,b; Ding et al., 2017, 2020). Using numerical simulations, previous authors have studied the dissolution-precipitation process of minerals at the pore scale under different CO_2 pressures and concluded that the precipitation reaction depends on the anisotropy of the rock structure surface and local material transport mechanism; the strongest dissolution occurs at the fluid inlet, and preciptation may block the fluid outlet (Wellman et al., 2003; Luquot et al., 2016). Molins et al. (2014) combined experimental, tomographic, and porous computational techniques to simulate water-carbonate rock interactions at 4 bar pCO_2. They examined the pore-scale mass transfer and surface reaction processes during calcite dissolution under high pCO_2 conditions. Deng et al. (2013, 2015, 2016) proposed a 2.5D continuous reactive transport model that captures and predicts the spatial pattern of the fracture pore size variation and the development of alteration layers in the near-fracture region. They observed the preferential dissolution of calcite in dolomite fractures, which results in the formation of preferential flow channels and altered layers. Garcia-Rios et al. (2015, 2017) conducted CO_2 fluid-fractured limestone/sandstone core flooding experiments, established a two-dimensional (2D) reaction transport model, and clarified that an increase in the flow rate led to an increase in the volume of dissolved limestone per unit time, indicating that the rate of calcite dissolution in fractures is controlled by transport. The rate of calcite dissolution was calculated by Noiriel et al. (2020) through XMT characterization by observing the dissolution/precipitation characteristics of the three-dimensional (3D) surface of the mineral crystals. Future research should upgrade the pore-scale simulation to the site scale and even basin scale through numerical simulation combined with core CT characterization to provide solutions for oil and gas exploration/carbon sequestration (Steefel et al., 2005, 2018; Noiriel et al., 2009, 2018, 2021). These studies have deepened understanding of CO_2-fluid-rock interactions at different levels, but they are insufficient for deep and ultradeep carbonate reservoirs. The studies above cannot explain the genesis mechanism of deep and ultra-deep fractured carbonate reservoirs because of the long duration of the water-rock interaction time, high temperature and pressure, and complex fluid composition under the geological background.

Based on the geological background of deep and ultra-deep fractured carbonate reservoirs in the Shunbei oil and gas field, the objective of this study was to investigate the interactions between fractured carbonate reservoirs and brine with dissolved CO_2 under surface-deep strata conditions and the influence of these interactions on fractured carbonate reservoirs. Specifically, we carried out a series of reactions of fractured carbonate core samples in brine with dissolved CO_2 from atmospheric to high temperatures and pressures (T = 50–200 °C, P = 10–60 MPa). Microscopy, SEM and spectral measurements, XCMT scanning, fluid chemistry analysis, and TOUGHREACT numerical simulations were used to qualitatively and quantitatively characterize changes in the fracture area and volume, sample porosity and permeability, calcite dissolution amount, calcite saturation index, calcite dissolution rate, and cation concentration in the fracture before and after the reaction with an acidic solution. The influence of heterogeneity and fluid flow on the fracture-fluid-rock interaction was explored, and thus the conditions and locations favorable for reservoir formation were clarified.

2. Physical experiment

2.1. Sample characterization

The sample used in the experiment was limestone from the Ordovician Yijianfang Formation of the Yijianfang section of the Tarim Basin. Microscopic observation of the thin section identified the lithology as micritic limestone containing bioclastic clusters (Fig. 1). The X-ray diffraction whole-rock analysis of the sample showed that the minerals consisted mainly of calcite (81.3%), common pyroxene (18.0%), and quartz (0.7%) (model: Panalytical X'Pert PRO, X-ray diffractometer, Institute of Nuclear Industry). Six core samples with a diameter of 2.5 cm and a length of approximately 6 cm were cored side by side in one limestone sample. The core samples were relatively compact, with porosity ranging from 0.62% to 2.33% and permeability ranging from 0.693×10^{-3} to 1.300×10^{-3} μm^2 (model: 3H-2000-HPK, Multifunctional Gas Permeability Instrument, Chinese Academy of Sciences). A longitudinal fracture was created artificially by sawing each core with a saw. An initial fracture aperture was between 0.8 mm and 1.0 mm depending on the sample, and obtained from XCMT observation (refer to Garcia-Rios et al., 2015; Hang Deng et al., 2018 for the fracture creation). The core samples were rinsed with deionized water, dried in an oven at 105 °C, weighed, and then wrapped with a heat-shrink film.

2.2. Experimental equipment

Six flow-through experiments with fractured cores were performed using the high T/P fluid-rock interaction equipment independently developed and designed by our research institute. Simulation experiment of the gas-liquid-solid phase were performed under normal temperature/pressure to high temperature/pressure. The device consists of the following parts: core holder, pressure vessel, constant-flow and constant-pressure pump, confining pressure pump, and effluent collection device. The experimental conditions, such as temperature and pressure, were monitored and controlled using a computer in real time. The fluid pressure at the inlet of the holder can be tracked by a confining pressure pump (the pressure difference is constantly larger than 5 MPa) to ensure that the fluid is transported in the pores inside the core. Then, a constant-flow pump is used to set a constant flow rate to drive the fluid

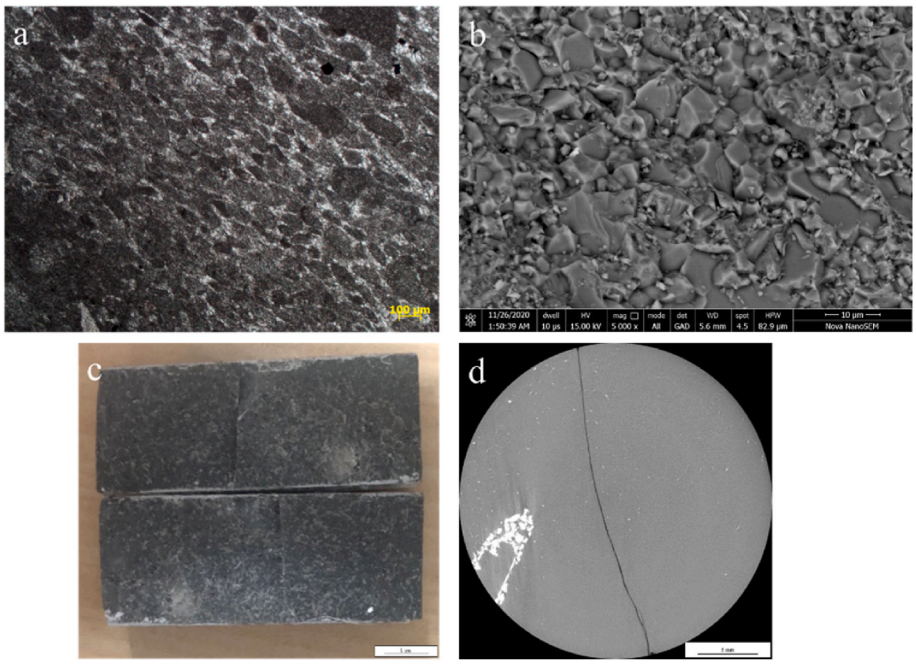

Fig. 1. Yijianfang Formation in the Yijianfang section of the Tarim Basin: a. Microscopic features: micritic limestone containing bioclastic clusters; b. SEM shows that the fracture surface morphology of the sample is compact; c. The core sample RS 3–10 after cutting along the long axis; d. X-ray computed microtomography (XCMT) scans of the core sample RS 3–10 after sawing (top view).

flow inside.

The main technical specifications of the equipment were as follows: the experimental simulation temperature range was from room temperature to 500 °C, the pressure range was from atmospheric pressure to 100 MPa, and the flow rate range was 0.01 mL/min–10.00 mL/min. The core holder could load core samples with a diameter of 2.5 cm for a temperature range from room temperature to 200 °C and a pressure range was from atmospheric pressure to 100 MPa. The device can simulate the process of gas-fluid-rock interaction under different temperature and pressure conditions and quantify the dissolution effect of geological fluid on carbonate reservoirs under different burial depths (corresponding to different T/P) (Fig. 2).

2.3. Experimental methods

The experimental methods were as follows. A solution of the simulated formation fluid was prepared using deionized water containing 20 wt% NaCl, and pure CO_2 gas was bubbled into the pressure vessel for 24 h to reach full equilibrium under different experimental pressures. CO_2 in geological fluids originates from the crust or mantle, and is usually associated with volcanic activity, deep fractures, or hydrothermal fluid and mineral interactions (Ballentine et al., 2001; Liu et al., 2017). The magmatic activity in the Tarim Basin was more intense during the Hercynian period, and the magma-driven hydrothermal fluids carried CO_2 from the deeper strata. Previous studies have demonstrated that Laser Raman Spectroscopy shows that fluid inclusions in the Ordovician formation contain natural CO_2 (Chen et al., 2015). The fluid salinity setting refers to the analysis of fluid inclusions in the Yijianfang Formation in the Tarim Basin, with the highest salinity in the Shunbei area reaching 22.4 wt% NaCl (Wang et al., 2019). The fluid is from the deep strata and has been in contact with the strata for a long time. Thus, the experimental fluid salinity was set as 20 wt% NaCl. Core samples wrapped in a heat-shrink film were assembled in a core holder. The main target was the Ordovician Yijianfang Formation in the Shunbei area of the Tarim Basin, where the burial depth currently exceeds 7000 m. To simulate the dynamic flow of fluid downward/upward along the fracture while reacting with the surrounding carbonate rock, we used a range corresponding to a formation depth from 1000 to 8000 m. The depth was converted to the reaction temperature and pressure based on the geothermal gradient (3 °C/100 m) (refer to Wang et al., 2014 for the

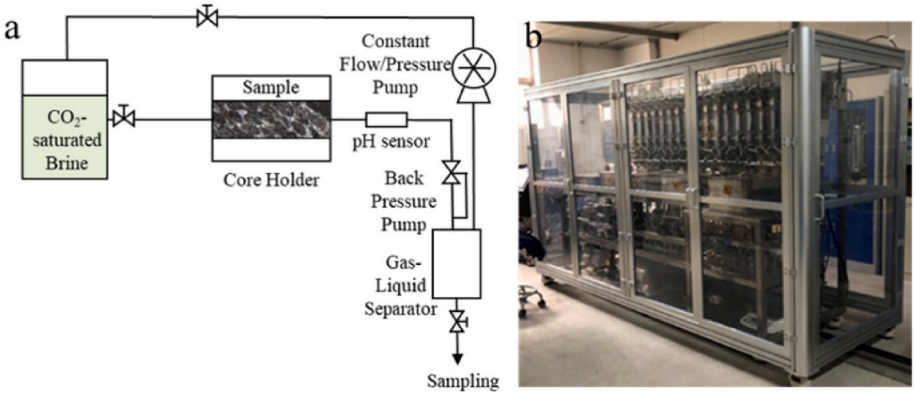

Fig. 2. High T/P fluid-rock interaction equipment: (a) schematic of the experimental setup; (b) Equipment appearance.

geothermal setting), with a temperature range from 50 to 200 °C and a pressure range from 10 to 60 MPa (Table 1). The reaction time for each sample was 24 h. At the beginning of the experiments, the fluid was pumped into the experimental system at a flow rate of 0.5 ml/min using a constant flow and constant pressure pump (refer to Deng et al., 2015 for the flow rate setting). The fluid flowed through the core holder through the main fracture and reacted with the fracture surface minerals (Table 1). Sample RS 3-1 was used as an example to estimate the residence time of the fluid in the core (only the fluid flow processes were considered), and the resident time was approximately 0.3 min. When the effluent fluid flowed out from the equipment outlet, it was collected every hour using a sampling tube, and the fluid pH was measured using a pH electrode (Orion, PEPRIS) at room temperature. The concentrations of Ca^{2+}, Mg^{2+}, and HCO_3^- in the fluid were measured by ICP-OES (5300DV plasma emission spectrometer, Institute of Nuclear Industry) and an alkalinity meter (AT-510 Fully Automatic Titration Analyzer, Institute of Nuclear Industry). The detection limits of Ca^{2+} and Mg^{2+} were 0.3 and 0.1 μg/L, respectively. The samples were removed after the experiments and washed three times with deionized water, dried in an oven at 105 °C for 24 h, weighed, and scanned by XCMT and SEM.

2.4. Fracture geometry characterization

Before and after the experiment, the cores were scanned using XCMT equipment (NanoVoxel 3502 E, Sanying Precision Instrument Co., Ltd.) The XCMT scan system was set to 170 kV (voltage), 100 μA (current), and 0.4 s (exposure time). The XCMT device has a plate detector of 1920 × 1536 pixels. The X-ray beam width ("slice" thickness) is 14.28 μm. A total of 1000 2D slices with pixels of different gray values were obtained using the built-in reconstruction algorithm of the CT system. All the slices were integrated in the ORS Visual SI software to reconstruct 3D space images and visualization. The pore network of the core 3D imaging data was extracted using ORS Visual SI to obtain the total number of pores, total number of throats, pore diameter, and throat diameter. The volume and area of the main fracture were extracted and calculated using VGSTUDIO MAX 3.4 software. Scanning electron microscopy-energy dispersive spectroscopy (SEM-EDS) was used to observe changes in the surface morphology of the samples before and after the experiment (Zeiss EVO MA 10, Germany, Institute of Nuclear Industry).

3. Experiment simulation

3.1. Modelling tool

Numerical simulations have become an established method for evaluating the degree of porous rock-CO_2 bearing fluid interaction. The numerical simulation results can be compared with physical experiments to predict the experimental results. At the same time, numerical simulations can examine experimental processes that cannot be observed in real time or directly and can be used to investigate changes in the fluid-rock reaction system at more minor spatial scales (e.g., changes in the mineral dissolution-precipitation interface, flow processes at the pore scale, etc.), and longer time scales (hundreds of days or even tens of thousands of years) (Hang Deng et al., 2019).

Table 1
Experimental parameters of the fracture-fluid-rock interaction simulation experiments.

Sample NO.	Burial depth/m	Surface temperature/°C	Temperature/ °C	Pressure/ MPa
RS 3-1	1000	20	50	10
RS 3-7	2000	20	80	20
RS 3-9	3000	20	110	30
RS 3-16	4000	20	140	40
RS 3-12	5000	20	170	50
RS 3-10	6000	20	200	60

The numerical simulation software TOUGHREACT was used in this study. TOUGHREACT is a good non-isothermal multiphase fluid reaction geochemical migration simulation software used for saturated or unsaturated media. It can simulate the flow, heat, multicomponent solute transport, and geochemical processes in one-, two-, and three-dimensional porous or fractured media during reservoir diagenesis. TOUGHREACT effectively combines water-rock interaction modeling with solute migration to model cementation, metasomatism, dissolution, pore destruction and preservation, pore filling composition, etc.(Xu et al., 2006). Unlike physical experiments, which are difficult to reproduce and whose scale is limited, numerical simulations performed with TOUGHREACT have almost no restrictions with regard to their time scales and spatial scales, or other conditions (Yang et al., 2022, 2022, 2022b a, 2022).

3.2. D conceptual model

Based on the above experiments, TOUGHREACT was used to simulate the experimental process. The calculation steps were as follows: 2D gridding with the experimental settings and the equal volume principle; setting fluid and water chemical parameters; assigning a value to the permeability of each grid; and outputting the ion concentration and mineral change of each grid in 24 h.

We cut the profile of the core in the simulation to observe fluid flow, transport, and reaction along the fracture. The profile in the model was the same as that in the experimental situation and was based on the CT data. Therefore, comparing the simulated profile results with actual CT data can accurately capture the flow characteristics of the fluid along the fracture. The core of the simulation was 6.5 cm long and 2.2 cm wide (to reduce on the calculation time, the width was reduced by 0.3 cm, which parallels that of the main fracture). The main fracture surface was tiled along the X- and Y-axes, and the fluid flowed from left to right along the X-axis. The total length in the x-axis direction was 6.5 cm, evenly divided into 200 grids, and the length of each grid was 0.0325 cm. The full length along the Y-axis direction was 2.2 cm, evenly divided into 40 grids, and the length of each grid was 0.055 cm. The length along the Z-axis direction was 2.2 cm with one grid. Therefore, the model comprised 8000 grids (Fig. 3).

3.3. Water chemistry

According to the experimental setting, the fluid in the simulation was a CO_2-brine containing 20 wt% NaCl by mass. The concentrations of H^+, Ca^{2+}, Na^+, K^+, HCO_3^-, and Cl^- in the fluid, and the pH of the fluid were measured under six temperature and pressure conditions (Table 2).

3.4. Initial conditions

Assuming that each initial formation is homogeneous, the parameters are listed in Table 3.

Cases 1–6 were homogeneous models in which the minerals were uniformly distributed in calcite. The sample XRD results reveal that there are still some silicon ions that do not react with the acidic fluid;

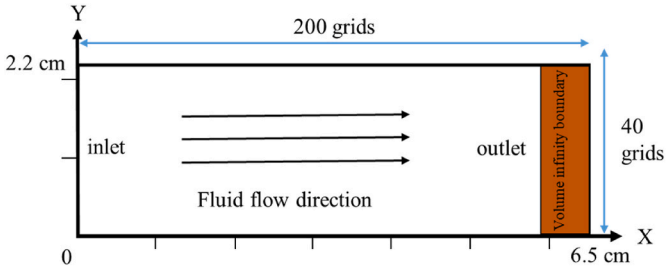

Fig. 3. Schematic of geological model subdivision.

Table 2
Initial ion concentrations in fluid under six temperature and pressure conditions.

Ionic Species	RS 3-1 50 °C 10 MPa	RS 3–7 80 °C 20 MPa	RS 3–9110 °C 30 MPa	RS 3–16 140 °C 40 MPa	RS 3–12 170 °C 50 MPa	RS 3–10 200 °C 60 MPa
$H^+/(10^{-3}$ mol/L)	1.1740	1.0270	1.1300	0.8928	0.7483	0.6118
pH	3.1340	3.1040	3.2549	3.2720	3.3320	3.7180
$Ca^{2+}/(10^{-4}$ mol/L)	0.2288	0.2822	0.2822	0.3474	0.3430	0.1246
Na^+/(mol/L)	2.1590	2.3010	2.4260	2.1850	1.9760	1.9780
$K^+/(10^{-3}$ mol/L)	0.7163	0.2687	0.2548	0.2595	0.2351	0.2284
$HCO_3^-/(10^{-3}$ mol/L)	0.7832	0.8049	0.9469	0.8189	0.7878	0.7368
Cl^-/(mol/L)	2.1590	2.3010	2.4260	2.1850	1.9760	1.9780

Table 3
Parameters related to the physical properties of the model.

Parameters	Value
Porosity (%)	2.00
Coefficient of compressibility (/Pa)	4.5×10^{-10}
Rock density (kg/m^3)	2650
Thermal conductivity [W/(m·°C)]	2.51
Specific heat of rock particles [J/(kg·°C)]	920

therefore, they are not considered in the model. The flow velocity was set to 1.0417×10^{-6} m/s. The flow velocity in the model was converted from the experimental flow velocity relative to the cross-sectional area and the volume of the injected grid. This flow rate was consistent with the experimental injection velocity. In addition, the left middle area is the injection grid, which is consistent with the experimental injection fracture, and the core and fracture permeabilities were set according to the test results. The matrix permeability of the RS 3-1 sample was 1×10^{-15} m^2, and the fracture permeability was 1.2×10^{-11} m^2.

The model permeability images at time 0 for the six cases were compared with the XCMT scan core profiles. The position of the model permeability was consistent with the core fracture morphology.

3.5. Boundary conditions

The left side of the model was a constant velocity injection boundary, and the right side was a constant pressure boundary, which ensured that the fluid could be injected into the grid at all times. All physical and chemical conditions, such as the pressure and ion concentration of the boundary, which not only provided internal pressure in the evacuation system but also simulated the infinite spatial scale of the actual formation, did not change with time.

4. Results

A series of simulation experiments were conducted according to the experimental scheme. The differences before and after the reaction were qualitatively and quantitatively compared in terms of the mass loss percentage, dissolved cation concentration, pH, changes in physical properties, reservoir space morphology, fracture area, and fracture volume.

4.1. Aqueous chemistry

The reaction system includes CO_2-brine (the fluid contained CO_2 (sc/g), CO_2 (aq), HCO_3^-) and calcium carbonate. CO_2 enters the brine, and the following reactions occur:

$$CO_2(gas) \leftrightarrow CO_2(aq)$$

$$CO_2 + H_2O \leftrightarrow H_2CO_3$$

$$H_2CO_3 \leftrightarrow H^+ + HCO_3^-$$

$$HCO_3^- \leftrightarrow H^+ + CO_3^{2-}$$

$$H_2O \leftrightarrow H^+ + OH^-$$

Calcium carbonate dissolution occurred in the core holder：

$$CaCO_3 + H^+ \rightarrow Ca^{2+} + HCO_3^-$$

The time-varying dissolved Ca^{2+} concentrations of the six cores are given in Fig. 4.

The dissolved cations included Ca^{2+}, Mg^{2+}, Na^+, K^+, and Ca^{2+}. The cation concentration fluctuated with experimental conditions and time, reflecting the influence of the experimental conditions (temperature and pressure) and fracture development. Among them, the dissolved Ca^{2+} concentrations and the fluctuation ranges of RS 3–7 and RS 3–9 were larger. The follow-up XCMT scan results revealed that the fractures of the above two samples were relatively straight, and their fluid flow rates were less affected by the branch fractures than those of the other samples.

The relationship between fluid pH and time during the reaction is shown in Fig. 5.

In the above six experiments, after the acidic solution reacted with the cores, the fluid pH increased by approximately 1.55–2.60 and then slowly decreased to a stable value. The fluid-rock reaction reaches equilibrium when the concentration of ions, such as Ca^{2+} and H^+ in the effluent reaches a constant value. As can be seen in Fig. 5, the pH of the effluent from each sample tended to stabilize after 16 h, indicating that the interaction between the mineral and the fluid in the reactor tended to be in equilibrium. The Ca^{2+} concentration (excluding individual fluctuation points) in Fig. 4 also reflects this trend.

4.2. Relationship between mass loss and temperature

We weighed the mass of the six cores before and after they reacted with the acidic solution, and calculated and compared the dissolution mass loss percentages under different temperatures (mass loss percentage = (mass before reaction – mass after reaction)/mass before reaction × 100%).

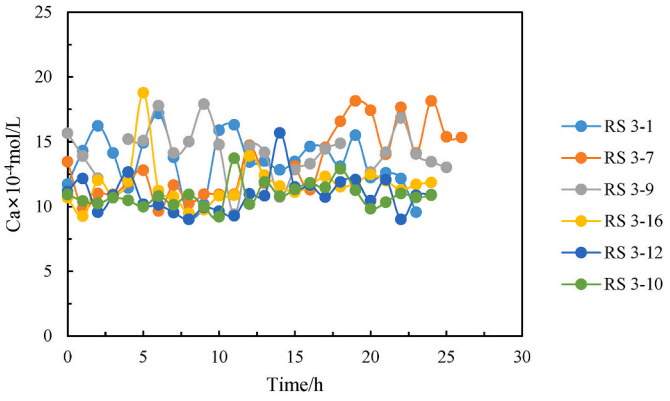

Fig. 4. Variation in the Ca^{2+} concentration with time.

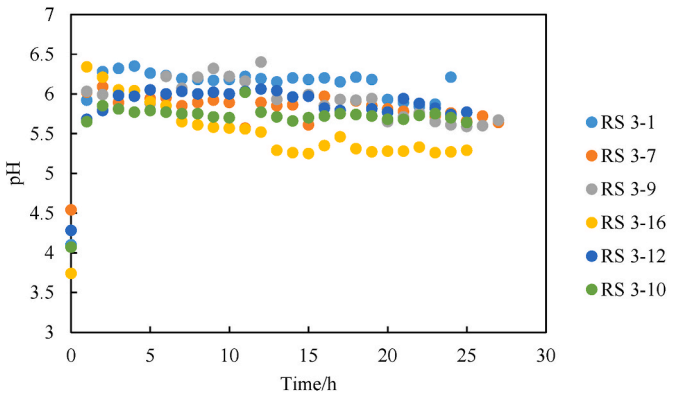

Fig. 5. Variation in the fluid pH with time.

The experimental results revealed that the acidic fluid has a noticeable dissolution effect on carbonate rocks, and the mass loss percentage of dissolution was in the range of 1%–2%. The mass loss percentage of the cores increased gradually with increasing temperature and then decreased at 170 °C. The mass loss percentage of RS 3–12 (170 °C) was 1.8 times higher than that of RS 3-1 (50 °C)(Table 4).

4.3. Fracture surface morphology changes

The morphological changes in the main fracture surfaces of the cores before and after the reaction were compared in situ using SEM (Fig. 6). The process and degree of dissolution and transformation of the fractures by the fluid under different temperatures and pressures were qualitatively evaluated by observing the morphological changes of pores, cavities, fractures, and crystal surfaces.

Before the experiment, the size of the calcite particles was relatively uniform, the interior and the crystal edge were complete, and there were no etch pits or other dissolution features on the crystal surface (Fig. 6 a, b). After the experiment, a large number of honeycomb-like etch pits appeared on the crystal surface, and the diameters of the pores were 10 μm–70 μm. The dissolution was enhanced along the contact edges of the calcite particles. The curvature of the crystal edges increased, forming dissolution fractures and etch pits (Fig. 6 c, d, e,f). The enhancement of local dissolution promotes the formation and connection of pores and fractures, thereby increasing the surface roughness and overall heterogeneity. The reaction time for each core was 24 h, and no new mineral precipitation was observed on the surface after the reaction.

On the crystal scale, the dissolution of surface asperities, such as steps, crystal edges, and corners, was faster than the average surface retreat because of the formation of many steps on the crystal surface. As a result, the flat cleavage surface gradually evolved into a curved surface, and the crystals became more rounded over time. In contrast, the topographic lows and bottoms of the steps dissolve more slowly than in the surrounding areas (Noiriel et al., 2020).

Table 4
Mass loss rate of samples during the reaction.

Sample NO.	Temperature/ °C	Pressure/ MPa	Mass Before Reaction/ g	Mass After Reaction/ g	Mass Loss Percentage/ %
RS 3-1	50	10	81.6151	80.7934	1.007
RS 3-7	80	20	86.1441	84.9705	1.362
RS 3-9	110	30	81.0798	80.2186	1.062
RS 3-16	140	40	66.4589	65.9893	0.707
RS 3-12	170	50	82.0866	80.5501	1.872
RS 3-10	200	60	46.3913	45.7642	1.352

4.4. Fracture area/volume calculated from XCMT

The cores were scanned using XCMT before and after the experiment. Through threshold segmentation of 3D images, the pores and matrix, for example, were separated. A binary dataset in which zero and one were used to represent the pore and matrix, respectively, was generated (Jiang et al., 2017). The areas and volumes of the main fractures were then calculated. The physical characteristics of the fractures, such as thickness and shape, before and after the reaction were determined (Fig. 7).

To avoid the influence of confinement pressure on the fracture, we used a heat-shrink film to wrap the sample before the experiment. The heat-shrink film can closely wrap and fix the two halves of the cut core sample after heating, which can minimize the relative movement during the assembly process and offset the influence of the confinement pressure. Second, the images scanned by CT before and after the experiment were calibrated, and the relative positions of the images were consistent in all regions except for the fracture; therefore, the experimental data comparison could reflect the relative changes in the fractures before and after the experiment. Third, we considered online CT scanning (Yang et al., 2022; Al-Khulaifi et al., 2019), but owing to the high temperature and pressure of the experiment and the large sample size, online real-time CT scanning could not be supported.

The degree of fluid transformation was compared by comparing the changes in the area and volume of the main fractures before and after the experiment (Table 5). The main fracture areas of RS 3-1 and RS 3–7 increased slightly, whereas the fracture area of the remaining samples decreased by more than 50%. Except for sample RS 3–9, the volume of the remaining samples increased by 1.2–4 times (corresponding to RS 3–16 and RS 3–7, respectively).

4.5. Pore diameter distribution before and after the experiment

According to the results of XCMT scanning, the diameters of all the pores in each core before and after the reaction were determined, and the number of pores in different diameter ranges was counted (Table 6). The distribution of pore diameters can reflect the degree of dissolution and transformation of pores of various sizes during the dissolution process. The dissolution process increased the diameter of the pores, and the precipitation process reduced the diameter.

From the pore diameter distribution of the six cores and the trend before and after the experiment, the pore diameter of the samples was mainly 25 μm–50 μm, accounting for 60%–75% of the total number of pores. The number of pores with diameters in the range 25 μm–50 μm increased substantially after the experiment. Thus, the increase significantly contributed to an increase in the total porosity.

4.6. Permeability and porosity change

For the binary image that divides the pores and matrix, the lattice Boltzmann method (LBM)–double relaxation time model (TRT) was used to calculate the permeability in the XYZ directions and the rate of change of permeability (Jiang et al., 2017). The direction along the fracture is in the X direction, and the Y and Z directions are the directions of the CT scan, which are not necessarily perpendicular to the X direction. Therefore, the main comparison was the rate of change in permeability along the Z-direction. The results revealed that the permeability of the cores increased after the experiment, among which the permeability of the RS 3–7 sample increased by approximately 26 times, the permeability of the RS 3–12 sample increased by approximately 39 times, and the permeability of the RS 3-1 sample increased by 74%. The permeability of RS 3-16 decreased slightly after the reaction (Table 7). The permeabilities of RS 3–9 and RS 3–10 after the reaction were unmeasurable, mainly because the dissolution process excessively expanded the fluid channels and caused the fractures to be disconnected.

The porosity of each core and porosity change before and after the

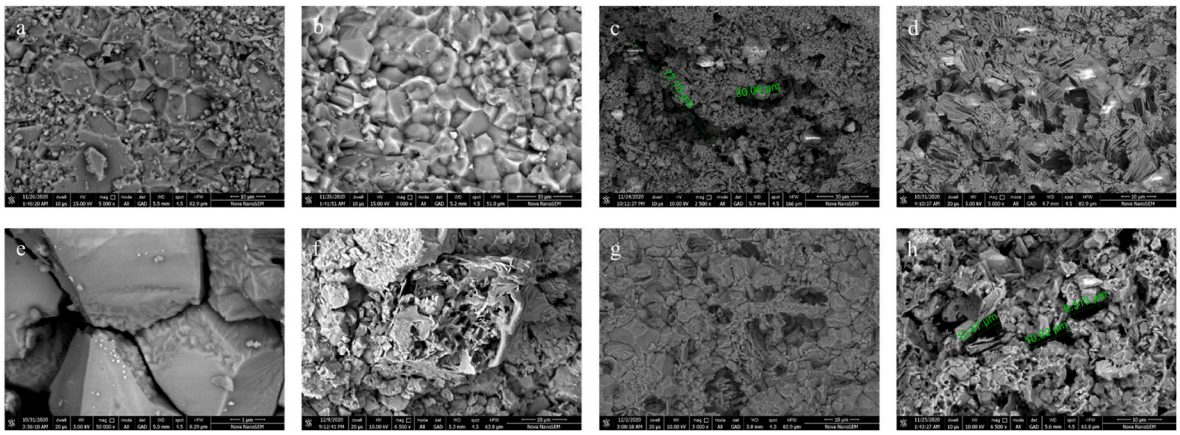

Fig. 6. Surface morphology characteristics of fractures in cores before and after the experiment (a,b limestone before reaction; c. RS 3-1 after reaction; d. RS 3–7 after the reaction; e. RS 3–9 after the reaction; f. RS 3–16 after the reaction; g. RS 3–12 after the reaction; h. RS 3–10 after the reaction).

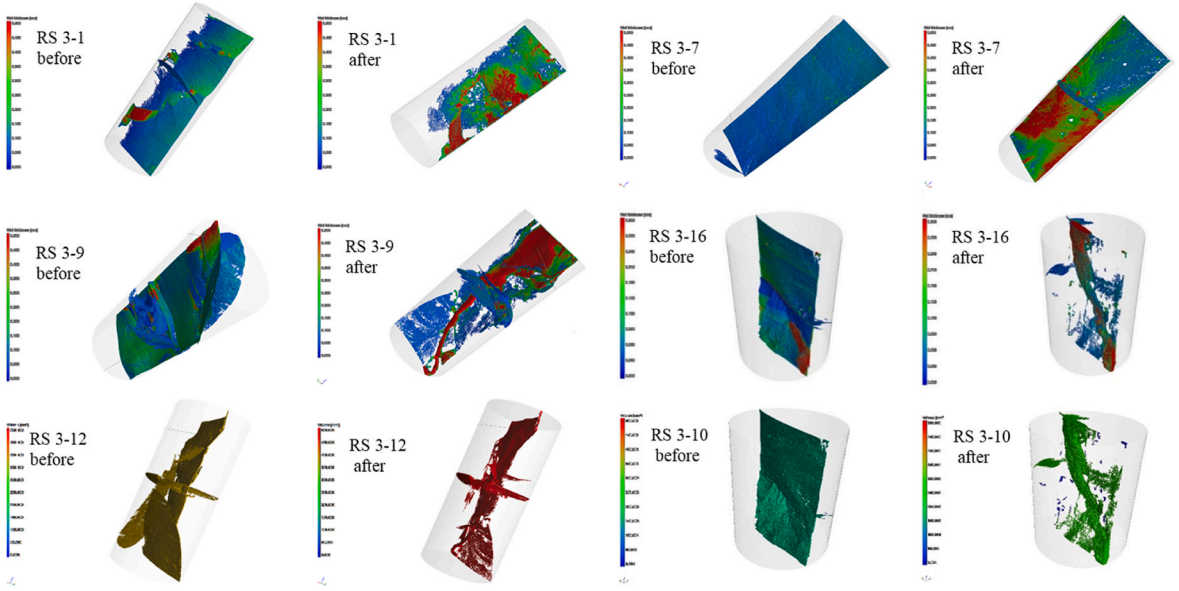

Fig. 7. Fracture morphology scanned by XCMT before and after the reaction.

Table 5
Area and volume changes of the main fractures before and after the experiment.

Sample NO.	Area Before Reaction/mm^2	Area After Reaction/mm^2	Volume Before Reaction/mm^3	Volume After Reaction/mm^2	Proportion of Fracture Volume Before Reaction	Proportion of Fracture Volume After Reaction
RS 3-1	3675.326	3696.807	145.326	280.514	0.67%	1.29%
RS 3-7	4953.806	5189.603	128.858	500.076	0.41%	1.62%
RS 3-9	6532.773	4453.342	253.261	217.692	0.84%	0.71%
RS 3-16	3163.258	1932.345	120.207	143.32	0.49%	0.59%
RS 3-12	11 528.248	6905.831	391.276	542.048	1.27%	1.78%
RS 3-10	4946.830	2454.505	156.486	293.596	1.07%	2.00%

experiment were calculated (Table 7). It can be seen that the porosity of the cores increased after the experiment and that of RS 3–7 increased by approximately three times. The porosity increases in the other samples ranged from 22% to 88%.

The porosity change rate exhibits a trend similar to that of the Ca concentration change in Fig. 4. RS 3–7 seems to have the highest dissolution. In Fig. 4, RS 3–7 shows a sudden increase in Ca concentration after 16 h. It is possible that the fluid made contact with a certain area with purer/more calcite, thereby increasing the reaction rate. In addition, the morphology of the fracture can cause fluctuations in the reaction process, and the bending of the fracture and branch fracture may affect the fluid flow, which in turn affects the reaction of H^+ and calcite. From the XCMT results, the fractures of RS 3–7 were the most uniform and flattest, and therefore the sample exhibited the highest degree of dissolution. According to Noiriel (2015), the process of mineral dissolution that releases metal ions from the lattice is not smooth and may be pulsed, which also causes fluctuations in the cation profile. Finally, based on the present data and simulation results, the effects of temperature and pressure on the dissolution and dissolution patterns were unclear. The reaction rates of calcite at different temperatures have

Table 6
Pore size distribution before and after the experiments.

	RS 3-1	RS 3-7	RS 3-9	RS 3-16	RS 3-12	RS 3-10
Pore Size Radius(μm) Before the experiments						
0–10	0.00%	0.00%	0.00%	0.00%	0.00%	0.00%
10–25	8.00%	0.70%	7.01%	7.23%	0.99%	0.73%
25–50	**64.92%**	**73.87%**	**70.36%**	**66.49%**	**59.56%**	**75.22%**
50–100	22.25%	2.48%	17.69%	19.29%	31.67%	18.19%
100–200	2.67%	22.30%	2.28%	4.56%	5.97%	3.67%
200–500	2.15%	0.66%	2.65%	2.40%	1.39%	2.17%
>500	0.01%	0.00%	0.01%	0.04%	0.43%	0.02%
Pore Size Radius(μm) After the experiments						
0–10	0.00%	0.00%	0.00%	0.00%	0.00%	0.00%
10–25	4.94%	0.96%	2.77%	4.75%	1.46%	5.01%
25–50	**66.66%**	**78.40%**	**81.17%**	**71.04%**	**65.36%**	**63.70%**
50–100	24.04%	5.62%	15.37%	21.25%	28.81%	25.28%
100–200	3.41%	12.06%	0.57%	2.82%	4.05%	4.89%
200–500	0.86%	2.55%	0.11%	0.12%	0.26%	1.02%
>500	0.10%	0.41%	0.01%	0.01%	0.07%	0.09%

been discussed and calculated in previous studies (Peng et al., 2015; Pokrovsky et al., 2009), and an increase in temperature can cause an increase in the reaction rate and reaction constants; however, the temperature-pressure effect is not obvious under actual multi-parameter reaction conditions.

4.7. Model results

4.7.1. Zero-time permeability

Based on the matrix permeability, fracture permeability, and XCMT scan results, the permeability distributions of the six core samples at the start of the experiment were set and calculated. The model results were consistent with the XCMT scan results (Fig. 8). The zero-time permeability comparison is used as a basis for the calculation of mineral composition, dissolved ions, and other parameters.

4.7.2. Spatial and temporal distribution characteristics of the mineral dissolution, calcite saturation index, and reaction rate in main fractures

Based on the initial conditions, the dissolved amount of calcite at 2 h (dissolved calcite mass/initial calcite mass), calcite saturation index, and calcite reaction rate in the main fracture under different experimental conditions within the reaction time were calculated (Fig. 9).

SI_c is the solubility product of calcite; IAP_c is the ionic activity product ($IAP_c = [Ca^{2+}][CO_3^{2-}]$). When $SI_c > 0$, the calcite precipitated. When $SI_c = 0$, calcite dissolution and precipitation reached an equilibrium. When $SI_c < 0$, calcite precipitated. $[Ca^{2+}]$ is the concentration of Ca^{2+} in the fluid (mol/L), and $[CO_3^{2-}]$ is the concentration of CO_3^{2-} in the fluid (mol/L).

The acid fluid migrated and flowed along the fractures and reacted with the surrounding rock. The degree of dissolution was highest at the entrance and gradually decreased along the flow path. The calcite saturation index characterizes the degree of dissolution; the more negative the saturation index, the higher the degree of calcite dissolution. This parameter showed a similar trend to the dissolved amount of calcite, and the overall reaction trend was dominated by dissolution. The calcite reaction rate also appeared to be related to the fluid hydraulic characteristics as well as the reaction temperature.

5. Discussion

We show the evolution of fracture geometry, geochemical reactions, and fracture hydraulic properties, focusing on the effects of structural heterogeneity and the relationship between dissolution and precipitation. The flow and reaction processes in the fractures promote and influence each other. Mineral dissolution and mineral precipitation alter the fluid channel morphology, porosity, and permeability of porous

Table 7
Permeability and porosity change before and after the experiments.

Sample No.	X-direction Permeability Before Reaction/D	X-direction Permeability After Reaction/D	Rate of Permeability Change	Porosity Before Reaction/%	Porosity After Reaction/%	Porosity Change
RS 3-1	12.3919	21.579	74%	1.52	2.39	57%
RS 3-7	2.43162	66.5925	2639%	0.62	2.61	321%
RS 3-9	12.3115	–	–	1.63	1.99	22%
RS 3-16	6.80515	6.24662	−8.2%	1.56	1.91	22%
RS 3-12	22.2947	901.302	3943%	2.33	4.38	88%
RS 3-10	5.84671	–	–	1.83	3.25	76%

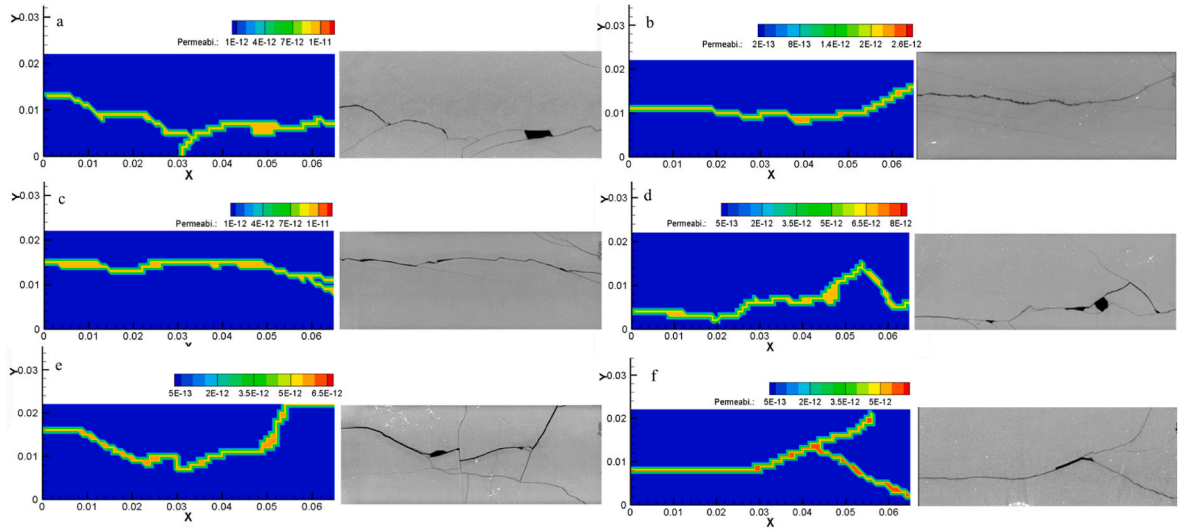

Fig. 8. Comparison of zero-time permeability and XCMT scanned profiles (a, RS 3-1; b, RS 3–7; c, RS 3–9; d, RS 3–16; e, RS 3–12; and f, RS 3–10).

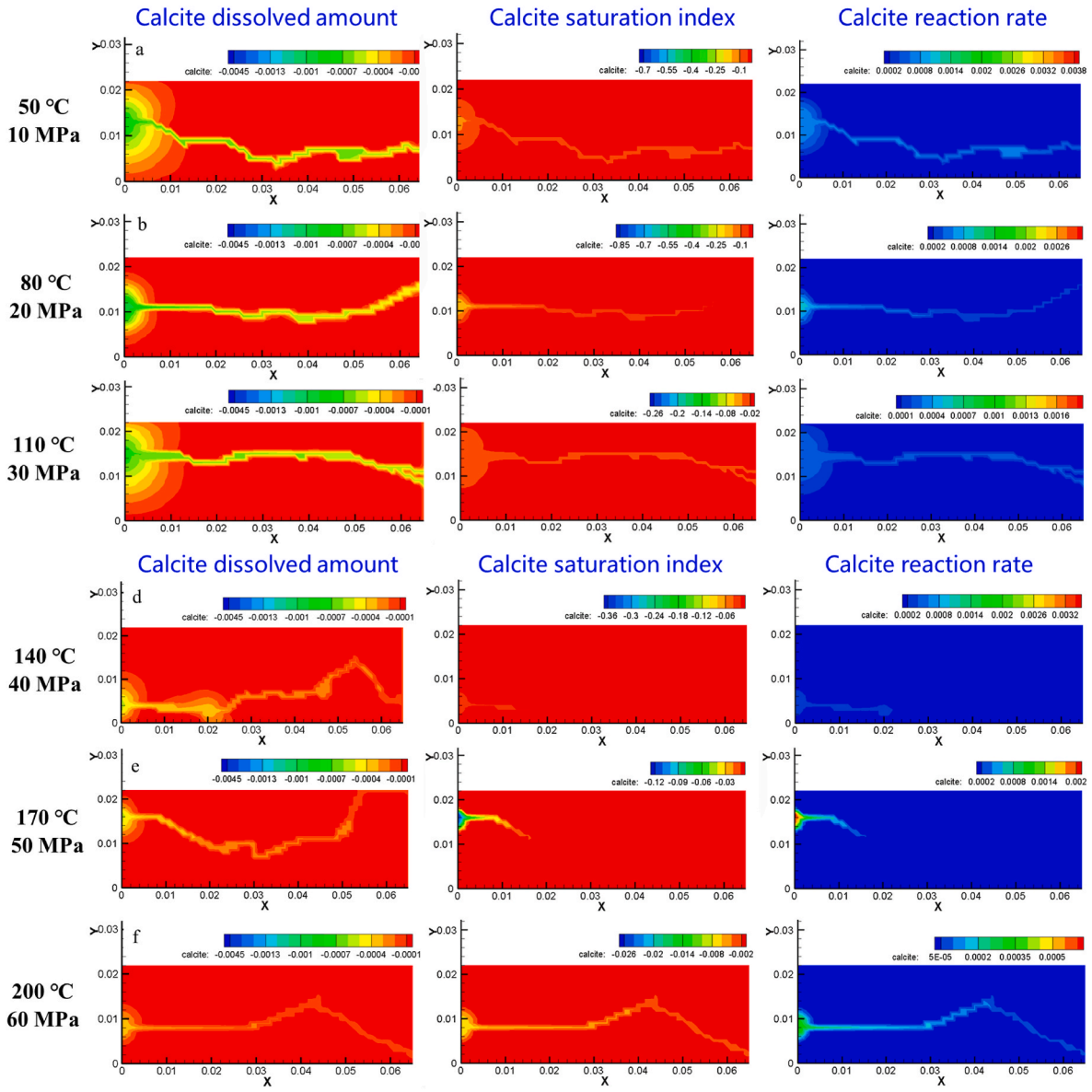

Fig. 9. Temporal and spatial evolution of the dissolved amount of calcite (first column), calcite saturation index (second column), and calcite reaction rate (third column) under different experimental conditions. (a, RS 3-1, 50 °C, 10 Mpa; b, RS 3–7, 80 °C, 20 MPa; c, RS 3–9, 110 °C, 30 MPa; d, RS 3–16, 140 °C, 40 MPa; e, RS 3–12, 170 °C, 50 MPa; and f, RS 3–10, 200 °C, 60 MPa).

rock, affecting the fluid flow process.

5.1. Distribution of calcite dissolved amount, calcite saturation in the fluid channels

The numerical simulation used a tracer to indicate the physical flow of the fluid in the channel, which did not include the chemical reaction process. The fluid entered the fracture from the inlet to the left and flowed along the fracture. Simultaneously, the fluid diffused perpendicular to the fracture plane (Deng and Spycher, 2019). The diffusion process spreads from the center to the circumference along the radius, and from the inlet to the outlet.

It calculates the temporal and spatial evolution of the amount of dissolved calcite. As the fluid flowed along the fracture, the dissolution of calcite started from the fracture and spread. The dissolution process has a significant hysteresis effect relative to the flow process of the fluid, which is caused by the co-coupling of the flow and reaction. Simultaneously, the fluid front migrated along the fracture and soon reached the outlet, and the fluid flow in the fracture also reacted with the minerals on the fracture surface. The dissolution reaction and degree of dissolution spread from left to right, from the inlet to the outlet, and the degree of dissolution at the inlet was always greater than that at the outlet.

It calculated the temporal and spatial evolution of the calcite saturation index under different experimental conditions. The initial calcite saturation index was zero, indicating neither dissolution nor precipitation. If dissolution occurred, the saturation index was negative; if precipitation occurred, the saturation index was positive. It was calculated that under the experimental conditions, the saturation index is negative, which means that only minerals dissolve in the reaction time. The calcite saturation index was most negative at the inlet. The degree of negative values gradually decreased along the fracture from left to right. The calcite saturation index approaches zero in the second half of the fracture. This shows that after the reaction at the front of the fracture, H^+ in the fluid is consumed, and the dissolution reaction at the back of the fracture becomes weaker. The numerical simulation of the reaction rate also shows a trend consistent with that of the calcite saturation index, which is due to the heterogeneity of the reaction rate. The presence of eddy currents in a rough cavity reduces the reaction rate on a large scale

(Deng et al., 2018; Noiriel and Soulaine, 2021).

The dissolved Ca^{2+} concentration calculated by numerical simulation was higher than the actual Ca^{2+} concentration. This comparison indicates that the reaction has not yet reached a complete equilibrium. The dissolution of calcite is diffusion-limited and far from equilibrium under acidic pH (Plummer et al., 1978; Rickard and Sjoberg, 1983). The premise of the calculation was an ideal system, and the reaction reached equilibrium. Second, the main fracture was dominated by the flow. The grains and fluids in the small pores away from the main fluid channel reached equilibrium and ion transfer through the diffusion boundary layer. This transport difference also causes discrepancies (Molins et al., 2014). Third, the THC model generally mimics the laboratory. Simulation results, with a range of numerical errors, were deemed reasonable. These errors are mainly due to several factors, such as rock sample heterogeneities and neglected adsorption (Yang et al., 2022a). The laboratory samples were real rock samples with a heterogeneous distribution of minerals, whereas the numerical simulation was based on XRD test results with uniform settings of mineral types and contents, so it is a spatially homogeneous state during the reaction. This cannot be avoided because in the experiment, we could not measure the specific distribution of each mineral grain. Fourth, the experimental sample had other small fractures in addition to the main fracture, including locations without fractures, and the physical properties were heterogeneous. Numerical simulations have tried to describe the real physical property distribution based on CT and other test data as much as possible, but after all, some microscopic phenomena are not experimentally tested and cannot provide information for numerical simulations. Finally, regarding the flow and reaction, there was a difference between the experiments and the numerical simulations. Experiments may cause turbulence owing to local blockage, instability of experimental parameters, etc. In contrast, the numerical simulation was purely computational, and there was no turbulence in the experimental conditions.

5.2. Sample heterogeneity changes

The homogeneity of a rock sample is determined by its composition and texture, that is, mineralogy and physical heterogeneity (Noiriel et al., 2018, 2021). Changes in the flow path geometry lead to the evolution of petrophysical parameters such as porosity, permeability, and surface area (Hoefner and Fogler, 1988; Daccord et al., 1993a, 1993b; Gouze and Luquot, 2011; Noiriel, 2015). Rock anisotropy (permeability anisotropy), pore-scale structural heterogeneity, and different mineral reactivities lead to new structural heterogeneity (Noiriel et al., 2007, 2015, 2021; Ellis and Bazylak, 2013; Garcia-Rios et al., 2017; Al-Khulaifi et al., 2019). The development of heterogeneous transport, which correlates advection-dominated flow paths with adjacent regions of static fluid dominated by diffusive transport, also facilitates nonlocal equilibrium at the pore scale (Noiriel and Soulaine, 2021).

5.2.1. Preferential flow channel formation

The composition of the core was relatively uniform and pure calcite was considered in the simulation. The drilled limestone cores are dense and uniform. The slightly different morphology of the main fracture facilitated the investigation of the effect of structural heterogeneity on the flow and reaction.

Owing to the high permeability of fractures, they act as preferential flow paths and thus generally control fluid flow and solute transport in fractured rocks (Deng and Spycher, 2019), whereas dissolution/precipitation primarily occurs in fractures (Garcia-Rios et al., 2015). The morphology and physical properties of fractures evolve dynamically with mineral dissolution and precipitation, driven by changes in fluid composition, temperature, and pressure (Deng and Spycher, 2019). The evolution of fracture pore size results from complex interactions between advection, diffusion, and surface reactions (Noiriel and Soulaine, 2021). The velocity distribution within the fracture was non-uniform, with fast and slow flow regions. In the advective-dominated transport regime, the faster flow path preferentially drives the reactants, resulting in non-uniform dissolution of the fractured surface, known as channeling (Starchenko and Ladd, 2018; Noiriel and Soulaine, 2021).

An artificially created fracture in the core is the dominant channel for fluid flow. After entering from the inlet, the fluid flows along the direction of the main fracture and dissolves the contact surface of the fracture, forming pores or expanding existing pores, expanding the main and branch fractures, and possibly precipitating minerals at the fracture ends (Andreani et al., 2009; Molins et al., 2014). The presence of the main flow channel makes the velocity field non-uniform, and the fluid velocity is reduced more (one to three orders of magnitude) in a non-channelized fracture (Noiriel et al., 2018). According to the theory of porous media seepage, the artificial fractures in the experiment were equivalent to creating wormholes along the flow direction. The corresponding dissolution pattern is a dominant wormhole dissolution with high Pe and high Da (Zhang et al., 2022). Wormhole formation increases rock permeability and flow heterogeneity, which, in turn, alters the dissolution dynamics of the fluid-rock interaction system (Daccord et al., 1993a,b). In this dissolution pattern, flow and dissolution in the fluid channel promote each other, and solute transport is dominated by advection and reaction, allowing rapid flushing of the dissolved solute around the isolated grain, which accelerates the dissolution process when more isolated grains are present (Zhang et al., 2022).

5.2.2. Evolution of the fracture area/volume

The results for the area and volume of the main fractures of the six cores showed that the volume and area increased after the reaction, and the volume increased more significantly (Table 5). The increase in the fracture area was due to the coupling between fluid flow and mineral dissolution. This coupling enhances the local porosity contrast, thus creating new surfaces for fluid-rock interactions. The pores and fractures formed by dissolution are connected and communicate with each other, which is conducive to the formation of dense and small fluid channels. This reduces the resistance of the fluid flow and provides more reaction sites for fluid-rock reactions. As in the previous sugar lump model (Noiriel et al., 2009), the accessibility of the fluid expands the fluid channel and enhances the degree of dissolution.

In the experiment, the acid fluid flowed through the fracture and reacted with the carbonate rock. After the reaction, the calcite grains on the fracture surface became smaller and the surface roughness increased. The fracture areas before and after the experiment were not much different, but the two cores' fracture areas are reduced by more than 50%. Correspondingly, the volume increases by 1.4–4 times after the experiments. Cores RS 3–12 and RS 3–10 exhibited smaller fracture areas and larger volumes after the experiments. The pressure of the core holder was increased from the normal pressure to 50 MPa, and the rubber sleeve further compacted the two halves of the core. The two faces of the fracture were pressed together to offset a part of the fracture area. Simultaneously, the fluid continues to flow through the uncompacted fractures, and the water-rock ratio is relatively increased. The fluid continued to dissolve the minerals and expand the volume of the fracture. Through similar fractured core percolation experiments and numerical simulations, the volume of the fracture increased 30–90 times at a flow rate of 1 ml/min (Deng et al., 2018).

Similarly, considering the effect of the fracture morphology on the dissolution process, the impact of the initial fracture geometry is secondary to the impact of the flow rate (Deng et al., 2018). Compared with core RS 3–12, the fracture of core RS 3–10 was straight and had a less negative effect on the main flow rate; therefore, the dissolution rate was higher (Noiriel and Soulaine, 2021). Therefore, the degree of reaction was higher, and the fracture volume increased. In general, in random fields with less roughness and shorter spatial lengths, fewer channels develop after the same reaction time. A decrease in the effluent cation concentration and overall dissolution rate was observed. A reduction in

the effluent cation concentration and overall dissolution rate was observed (Deng et al., 2018). In other words, the original structure of the fracture affects the way, path, and velocity of the fluid flow, which in turn affects the overall degree of dissolution. In summary, the factors affecting the fracture area/volume change include the hydrodynamic conditions, reaction pressure, and original geometry of the fracture.

5.2.3. Porosity changes

The changes in the porosity, permeability, pore diameter, pore amount, and other parameters of the six cores before and after the experiments were compared (Tables 6 and 7). After the reaction, the porosity of the cores increased, ranging from 22% to 321%, with an average increase of approximately 98%. Before the reaction, the calcium carbonate crystals were in close contact, the crystal edges were straight, and the crystal faces were flat. After the reaction, many etch pits and dissolved pores formed on the crystal faces, and dissolved channels formed between the edges of the individual crystals and contact surfaces. Fluid–rock reactions tend to occur in topographic highs, crystal edges and corners, etch pits, and rough areas of the crystal surface. The surface free energy of the above reaction positions is higher, and the dissolution/precipitation reaction is prone to occur (De Yorea., 2003; Ruiz-Agudo et al., 2013, 2014; Offeddu et al., 2014; Renard et al., 2018; Noiriel et al., 2018, 2020; Nooraiepour et al., 2021).

Noiriel et al. (2018, 2020) proposed that, during calcite dissolution in an acidic fluid, the dissolution rate of the crystal edge was estimated to be 1.7–2 times higher than that of the faces. Crystal edges may also experience higher diffusion fluxes at their surfaces, which are related to local hydrodynamic conditions. The dissolution rates significantly increased along the cleavage direction. Fine crystals will experience higher dissolution rates owing to more defects on the crystal surface and inside.

Mineral dissolution alters the pore structure by enlarging the throat diameter and reducing the pore specific surface area (Xu et al., 2017). The distribution of the pore diameter can reflect the degree of dissolution modification of pores of different sizes by the dissolution process, which enlarges the pore diameter and decreases the pore diameter by the precipitation process. Comparing the diameter and number of pores inside the core before and after the reaction, the pore diameter of the sample was mainly 25–50 μm, accounting for 60%–75% of the total number of pores. The number of pores with diameters of 25–50 μm increased after the reaction, which contributed significantly to the increase in total porosity, surface roughness, and reactive surface area.

When fluid flows in a porous medium, the changes in porosity and permeability are mainly determined by the large pores in the sample. When the dissolution reaction occurs in pores with a larger diameter, the overall porosity and permeability increase (Molins et al., 2014), which can also be understood as a positive feedback between the local permeability and mineral dissolution rate. This feedback constantly redirects less-saturated fluids to more permeable flow paths, further increasing their permeability. The fluid preferentially enters large pores with lower resistance and undergoes a dissolution/precipitation reaction. The greater the change in macropore diameter, the greater the change in the overall permeability. The results revealed that the number of pores with a diameter larger than 500 μm increased after the rock cores reacted with the acidic solution, and the permeability increased.

5.2.4. Permeability enhancement

Rock dissolution results in a highly complex and rough topography. The surface roughness increases locally owing to pit formation and coalescence (Steefel et al., 2015; Fischer and Luttge, 2018; Noiriel et al., 2018). Changes in sample surface roughness in an acidic environment lead to changes in absolute permeability (Pilotti et al., 2002).

The fracture of the cores in the experiments created preferential fluid channels, and the dissolution pattern corresponded to the dissolution of wormholes. The permeability enhancement after the experiment was also consistent with previous results (Luquot et al., 2013; Kaszuba et al., 2013; Garcia-Rios et al., 2015; 2017). Fracture channelization results in a rapid increase in fracture permeability, even under confining pressure, because the rough structure of non-channelized regions in the fracture is preserved and can prevent fracture closure (Deng et al., 2018). Simultaneously, the flowing particles can be transported by the flow without blocking the fracture or causing the fracture permeability to decrease. The direction and degree of the fracture permeability change depend on the interaction between dissolution and precipitation (Deng and Spycher, 2019). Rock dissolution increases the permeability of the sample, resulting in an increase in the overall connectivity (Saeed Abbasi, 2021).

After the experiment, the permeability of the core along the main fracture direction increased, and the increase ranged from about 26 to 39 times. The permeabilities in the other two directions also increased. This result is consistent with previous observations (Garcia-Rios et al., 2015; Deng et al., 2017; 2019; Noiriel and Soulaine, 2021). As the flow rate increased, the dissolution pattern changed from face dissolution to wormhole formation and uniform dissolution, and the fracture permeability always increased and depended on the type of dissolution pattern (Garcia-Rios et al., 2015).

The permeability of sample RS 3–16 was slightly reduced by 8.2%. Permeability reduction mechanisms include scale formation, suspended particle invasion, and fine particle migration (Saeed Abbasi, 2021). Based on the experimental setting, it is inferred that the migration of fine shed particles caused by upstream dissolution blocks the downstream micro-fractures (Luhmann et al., 2014; Luquot et al., 2014; Selçuk Erol et al., 2019). Fracture permeability increases with the detachment of the altered layer if the released particles are washed away (Deng et al., 2017, 2019), whereas if the released particles are redeposited in the fracture and cause a significant reduction in the fracture pore size, the fracture permeability will decrease (Noiriel et al., 2007; Ellis and Bazylak, 2013; Dávila et al., 2016; Deng and Spycher, 2019). In this study, because of branch fractures, flowing particles that were transported downstream by the fluid, where they could coalesce at narrow points and reduce the hydraulic permeability of the fractures (Noiriel et al., 2007; Ellis and Bazylak, 2013; Dávila et al., 2016 a).

5.3. Conditions for precipitation

In core observations of limestone formations, it is often observed that fractures or pores are cemented by calcite, which reduces the porosity and permeability of the reservoir and decreases the reservoir storage space. Therefore, it is important to understand the temperature, pressure, and fluid conditions under which calcite will dissolve or precipitate from formation fluids, or to clarify the depth (corresponding to T/P) in large-scale reservoirs.

Precipitation associated with fluid-mineral interface evolution and flow path reorganization also play an essential role in porous media (Tartakovsky et al., 2007a,b; Li et al., 2008; Noiriel et al., 2012; Noiriel and Daval, 2017; Godinho and Withers, 2018; Noiriel and Soulaine, 2021). In geological environmental studies, crystal nucleation and growth are critical for understanding the geometric evolution of porous media during reaction transport in geological environmental studies (Nooraiepour et al., 2021). During solute transport and reactive fluid flow within porous media, crystal nucleation and growth may alter the pore geometry and, thus, the transport properties of the porous media. Mineral precipitation and accumulation also change the reactive surface area for nucleation and growth, leading to changes in system reactivity and reaction rates.

According to mineral nucleation theory, faster nucleation occurs in the existing carbonate cement, etch pits, surface roughness, and crystal edges. These sites have higher surface free energy and thus attract mineral formation and growth (Nooraiepour et al., 2021). No new $CaCO_3$ precipitation was observed on the fracture surface by the SEM-EDS analysis, indicating a state of undersaturation in the fracture.

In a reaction system, the carbonation reaction changes the aqueous

species concentration, alkalinity, and pH of the pore solution in a relatively complex manner (Kashef-Haghighi et al., 2015; Sun et al., 2015; Pan et al., 2021). The pH of the acidic solution was less than 6; therefore, the main ions in the solution were H^+ and HCO_3^- (Edery et al., 2011). The process of surrounding rock dissolution is mainly the reaction between $CaCO_3$ and H^+ dissolved from CO_2. Ca^{2+} in the $CaCO_3$ crystal enters the solution and diffuses downstream with other ions such as H^+ and HCO_3^-. The CO_3^{2-} concentration depends on the pH of the pore solution and barely exists when the solution pH is less than 9. The precipitation reaction is also limited because of the lack of CO_3^{2-} when the solution pH is less than 9 (Anna Varzina et al., 2020).

During the experiment, the concentration of CO_3^{2-} in the fluid was very low (almost unmeasurable), and the concentrations of other cations, such as K^+ and Mg^{2+} was low neither. For example, the K^+ concentration is 20 mg/L-30 mg/L, and the Mg^{2+} concentration is approximately 2 mg/L-3 mg/L. The saturation of the corresponding carbonate minerals at this temperature was minimal, which was not sufficient to meet the precipitation requirement. Compared with other studies that observed calcium sulfate precipitation (Garcia-Rios et al., 2015; 2017), the initial solution was saturated with SO_4^{2-}, so it was easier to reach gypsum over-saturation and therefore precipitate gypsum. Increased calcium carbonate saturation and prolonged reaction time help increase the amount and total coverage of crystals (Nooraiepour et al., 2021). Transport limitations such as dead ends of fractures and less connected fractures (Singurindy and Berkowitz, 2005; Menefee et al., 2017), or slow flow velocity (Dávila et al., 2016a) favor precipitation and fracture closing (Deng and Spycher, 2019). In core observations of limestone formations, it is often observed that fractures or pores are cemented by calcite, which reduces the porosity and permeability of the reservoir and decreases the reservoir storage space. Therefore, it is important to understand the temperature, pressure, and fluid conditions under which calcite will dissolve or precipitate from formation fluids, or to clarify the depth (corresponding to T/P) in large-scale reservoirs.

If the fresh fluid supply is limited (slowing the flow rate and reducing the reactant concentration) or the reaction time is prolonged, the dissolution and precipitation reactions in the main fracture may reach equilibrium. Therefore, new mineral precipitation will be observed.

6. Conclusions

(1) An experiment was conducted to simulate fluid flow along the fracture, and the physical properties, area, and volume of the main fractures before and after the reaction were compared. The main factors controlling the main fracture area/volume change were the structural heterogeneity and hydraulic properties.
(2) The TOUGHREACT numerical simulation was used to calculate the temporal and spatial distributions of the main minerals, calcium carbonate saturation, and calcium carbonate dissolution rate in the main fracture. Calcium carbonate dissolved mainly during the reaction, and no new calcium carbonate precipitation occurred.
(3) The initial setup of the experiment (flow rate and sample fracture) promoted the formation of the main flow channels and wormhole dissolution pattern. The flow and reaction in the main flow channel promoted each other, and the existence of branch channels weakened the main flow rate. If the reaction time is sufficiently long, the end of the branch fractures or microfractures may be potential mineral precipitation sites.
(4) The development of fractured carbonate reservoirs is mainly determined by structural heterogeneity and hydraulic properties. Under the condition of a continuous fluid supply, if the fracture is wide and flat, it improves the reservoir storage performance. Significant fracture tortuosity and bifurcation weaken the modification effect of fluids and may lead to cementation, which will reduce reservoir storage performance.

Declaration of competing interest

The authors declare that they have no known competing financial interests or personal relationships that could have appeared to influence the work reported in this paper.

Data availability

Data will be made available on request.

Acknowledgment

This work was supported by the National Natural Science Foundation of China (42072177, U19B6003, and 42141011) and the Strategic Priority Research Program of the Chinese Academy of Sciences (XDA14010201),SINOPEC (P22207-1).

References

Abbasi, S., Khamehchi, E., 2021. Precipitation/dissolution and precipitants movement mechanisms effects on injectivity variations during diluted produced water re-injection into a layered reservoir-experimental investigation. Energy Sources, Part A Recovery, Util. Environ. Eff. 1–19.
Al-Khulaifi, Y., Lin, Q., Blunt, M.J., et al., 2018. Reservoir-condition pore-scale imaging of dolomite reaction with supercritical CO_2 acidified brine: effect of pore-structure on reaction rate using velocity distribution analysis. Int. J. Greenh. Gas Control 68, 99–111.
Al-Khulaifi, Y., Lin, Q., Blunt, M.J., et al., 2019. Pore-scale dissolution by CO_2 saturated brine in a multimineral carbonate at reservoir conditions: impact of physical and chemical heterogeneity. Water Resour. Res. 55 (4), 3171–3193.
Andreani, M., Luquot, L., Gouze, P., et al., 2009. Experimental study of carbon sequestration reactions controlled by the percolation of CO_2-rich brine through peridotites. Environ. Sci. Technol. 43 (4), 1226–1231.
Brantley, S.L., 2008. Kinetics of Mineral Dissolution [M]//Kinetics of Water-Rock Interaction. Springer, New York, NY, pp. 151–210.
Ballentine, C.J., Schoell, M., Coleman, D., et al., 2001. 300-Myr-old magmatic CO_2 in natural gas reservoirs of the west Texas Permian basin. Nature 409 (6818), 327–331.
Chen, H., Lu, Z., Cao, Z., et al., 2015. Hydrothermal alteration of Ordovician reservoir in northeastern slope of Tazhong uplift, Tarim Basin. Acta Pet. Sin. 37 (1), 43–63 (in Chinese).
Chen, L., Kang, Q., Carey, B., et al., 2014. Pore-scale study of Diffusion−Reaction processes involving dissolution and precipitation using the lattice Boltzmann method. Int. J. Heat Mass Tran. 75, 483–496.
Daccord, G., Lenormand, R., Lietard, O., 1993a. Chemical dissolution of a porous medium by a reactive fluid—I. Model for the "wormholing" phenomenon. Chem. Eng. Sci. 48 (1), 169–178.
Daccord, G., Lietard, O., Lenormand, R., 1993b. Chemical dissolution of a porous medium by a reactive fluid—II. Convection vs reaction, behavior diagram. Chem. Eng. Sci. 48 (1), 179–186.
Davies, G.R., Smith Jr., L.B., 2006. Structurally controlled hydrothermal dolomite reservoir facies: an overview. AAPG (Am. Assoc. Pet. Geol.) Bull. 90 (11), 1641–1690.
Dávila, G., Luquot, L., Soler, J.M., et al., 2016. Interaction between a fractured marl caprock and CO_2-rich sulfate solution under supercritical CO_2 conditions. Int. J. Greenh. Gas Control 48, 105–119.
Deng, H., Ellis, B.R., Peters, C.A., et al., 2013. Modifications of carbonate fracture hydrodynamic properties by CO_2-acidified brine flow. Energy Fuel. 27 (8), 4221–4231.
Deng, H., Molins, S., Steefel, C., et al., 2016. A 2.5 D reactive transport model for fracture alteration simulation. Environ. Sci. Technol. 50 (14), 7564–7571.
Deng, H., Fitts, J.P., Crandall, D., et al., 2015. Alterations of fractures in carbonate rocks by CO_2-acidified brines. Environ. Sci. Technol. 49 (16), 10226–10234.
Deng, H., Voltolini, M., Molins, S., et al., 2017. Alteration and erosion of rock matrix bordering a carbonate-rich shale fracture. Environ. Sci. Technol. 51 (15), 8861–8868.
Deng, H., Steefel, C., Molins, S., et al., 2018. Fracture evolution in multimineral systems: the role of mineral composition, flow rate, and fracture aperture heterogeneity. ACS Earth and Space Chem. 2 (2), 112–124.
Deng, H., Spycher, N., 2019. Modeling reactive transport processes in fractures. Rev. Mineral. Geochem. 85 (1), 49–74.
Ding, Q., He, Z., Zhang, J., et al., 2017. Factors controlling carbonate dissolution under high temperature and pressure, 04 Oil Gas Geol. 38, 784–791 (in Chinese).
Ding, Q., He, Z., Zhang, J., et al., 2020. Simulation Experiment of carbonate reservoir modification by source rock-derived acidic fluids, 01 Oil Gas Geol. 41, 223–234 (in Chinese).
Edery, Y., Scher, H., Berkowitz, B., 2011. Dissolution and precipitation dynamics during dedolomitization. Water Resour. Res. 47 (8).
Ellis, J.S., Bazylak, A., 2013. Investigation of contact angle heterogeneity on CO_2 saturation in brine-filled porous media using 3D pore network models. Energy Convers. Manag. 68, 253–259.

Erol, S., Fowler, S.J., Nehler, M., et al., 2019. An analytical algorithm of porosity–permeability for porous and fractured media: extension to reactive transport conditions and fitting via flow-through experiments within limestone and dolomite. Transport Porous Media 129 (1), 343–383.
Fischer, C., Luttge, A., 2018. Pulsating dissolution of crystalline matter. Proc. Natl. Acad. Sci. USA 115 (5), 897–902.
Garcia-Rios, M., Luquot, L., Soler, J.M., et al., 2015. Influence of the flow rate on dissolution and precipitation features during percolation of CO_2-rich sulfate solutions through fractured limestone samples. Chem. Geol. 414, 95–108.
Garcia-Rios, M., Luquot, L., Soler, J.M., et al., 2017. The role of mineral heterogeneity on the hydrogeochemical response of two fractured reservoir rocks in contact with dissolved CO2. Appl. Geochem. 84, 202–217.
Gouze, P., Noiriel, C., Bruderer, C., et al., 2003. X-ray tomography characterization of fracture surfaces during dissolution. Geophys. Res. Lett. 30 (5).
Gouze, P., Luquot, L., 2011. X-ray microtomography characterization of porosity, permeability and reactive surface changes during dissolution. J. Contam. Hydrol. 120, 45–55.
Godinho, J.R.A., Withers, P.J., 2018. Time-lapse 3D imaging of calcite precipitation in a microporous column. Geochem. Cosmochim. Acta 222, 156–170.
Han, C., Lin, C., Lu, X., et al., 2016. Characterization and genesis of fault-controlled karst reservoirs in Ordovician carbonate karst slope of Tahe oilfield, Tarim Basin, 005 Oil Gas Geol. 37, 644–652 (in Chinese).
He, Z., Zhang, J., Ding, Q., et al., 2017a. Factors controlling the formation of high-quality deep to ultra-deep carbonate reservoirs. Oil Gas Geol. 38 (4), 633–644, 763 (in Chinese).
He, Z., Ding, Q., Zhang, J., et al., 2017b. Experiment of carbonate dissolution: implication for high quality carbonate reservoir formation in deep and ultradeep basins. Geofluids 1–8, 2017.
Hoefner, M.L., Fogler, H.S., 1988. Pore evolution and channel formation during flow and reaction in porous media. AIChE J. 34 (1), 45–54.
Jiang, W., Lin, M., Yi, Z., et al., 2017. Parameter determination using 3D FIB-SEM images for development of effective model of shale gas flow in nanoscale pore clusters. Transport Porous Media 117 (1), 5–25.
Kashef-Haghighi, S., Shao, Y., Ghoshal, S., 2015. Mathematical modeling of CO_2 uptake by concrete during accelerated carbonation curing. Cement Concr. Res. 67, 1–10.
Kaszuba, J., Yardley, B., Andreani, M., 2013. Experimental perspectives of mineral dissolution and precipitation due to carbon dioxide-water-rock interactions. Rev. Mineral. Geochem. 77 (1), 153–188.
Li, L., Steefel, C.I., Yang, L., 2008. Scale dependence of mineral dissolution rates within single pores and fractures. Geochem. Cosmochim. Acta 72 (2), 360–377.
Li, W., Einstein, H.H., Germaine, J.T., 2019. An experimental study of matrix dissolution and wormhole formation using gypsum core flood tests: 1. Permeability evolution and wormhole geometry analysis. J. Geophys. Res. Solid Earth 124 (11), 11055–11073.
Liu, Q., Zhu, D., Jin, Z., et al., 2017. Effects of deep CO_2 on petroleum and thermal alteration: the case of the Huangqiao oil and gas field. Chem. Geol. 469, 214–229.
Lu, X., Wang, Y., Tian, F., et al., 2017. New insights into the carbonate karstic fault system and reservoir formation in the Southern Tahe area of the Tarim Basin. Mar. Petrol. Geol. 86, 587–605.
Luhmann, A.J., Kong, X.Z., Tutolo, B.M., et al., 2014. Experimental dissolution of dolomite by CO_2-charged brine at 100 °C and 150 bar: evolution of porosity, permeability, and reactive surface area. Chem. Geol. 380, 145–160.
Luquot, L., Gouze, P., 2009. Experimental determination of porosity and permeability changes induced by injection of CO_2 into carbonate rocks. Chem. Geol. 265 (1–2), 148–159.
Luquot, L., Rodriguez, O., Gouze, P., 2014. Experimental characterization of porosity structure and transport property changes in limestone undergoing different dissolution regimes. Transport Porous Media 101 (3), 507–532.
Luquot, L., Abdoulghafour, H., Gouze, P., 2013. Hydro-dynamically controlled alteration of fractured Portland cements flowed by CO2-rich brine. Int. J. Greenh. Gas Control 16, 167–179.
Luquot, L., Gouze, P., Niemi, A., et al., 2016. CO_2-rich brine percolation experiments through Heletz reservoir rock samples (Israel): role of the flow rate and brine composition. Int. J. Greenh. Gas Control 48, 44–58.
Ma, Y., Li, M., Cai, X., et al., 2020. Mechanisms and exploitation of deep marine petroleum accumulations in China: advances, technological bottlenecks and basic scientific problems, 04 Oil Gas Geol. 41, 655–672+683 (in Chinese).
Ma, Y., Cai, X., Yun, L., et al., 2022. Practice and theoretical and technical progress in exploration and development of Shunbei ultra-deep carbonate oil and gas field, Tarim Basin, NW China, 01 Petrol. Explor. Dev. 49, 1–17 (in Chinese).
Menefee, A.H., Li, P., Giammar, D.E., et al., 2017. Roles of transport limitations and mineral heterogeneity in carbonation of fractured basalts. Environ. Sci. Technol. 51 (16), 9352–9362.
Molins, S., Trebotich, D., Yang, L., et al., 2014. Pore-scale controls on calcite dissolution rates from flow-through laboratory and numerical experiments. Environ. Sci. Technol. 48 (13), 7453–7460.
Noiriel, C., Gouze, P., Bernard, D., 2004. Investigation of porosity and permeability effects from microstructure changes during limestone dissolution. Geophys. Res. Lett. 31 (24).
Noiriel, C., Bernard, D., Gouze, P., et al., 2005. Hydraulic properties and microgeometry evolution accompanying limestone dissolution by acidic water. Oil Gas Sci. Technol. 60 (1), 177–192.
Noiriel, C., Madé, B., Gouze, P., 2007. Impact of coating development on the hydraulic and transport properties in argillaceous limestone fracture. Water Resour. Res. 43 (9).
Noiriel, C., Luquot, L., Madé, B., et al., 2009. Changes in reactive surface area during limestone dissolution: an experimental and modelling study. Chem. Geol. 265 (1–2), 160–170.
Noiriel, C., Steefel, C.I., Yang, L., et al., 2012. Upscaling calcium carbonate precipitation rates from pore to continuum scale. Chem. Geol. 318, 60–74.
Noiriel, C., 2015. Resolving time-dependent evolution of pore-scale structure, permeability and reactivity using X-ray microtomography. Rev. Mineral. Geochem. 80 (1), 247–285.
Noiriel, C., Daval, D., 2017. Pore-scale geochemical reactivity associated with CO_2 storage: new frontiers at the fluid–solid interface. Acc. Chem. Res. 50 (4), 759–768.
Noiriel, C., Deng, H., 2018. Evolution of planar fractures in limestone: the role of flow rate, mineral heterogeneity and local transport processes. Chem. Geol. 497, 100–114.
Noiriel, C., Oursin, M., Saldi, G., et al., 2018. Direct determination of dissolution rates at crystal surfaces using 3D X-ray microtomography. ACS Earth and Space Chem. 3 (1), 100–108.
Noiriel, C., Oursin, M., Daval, D., 2020. Examination of crystal dissolution in 3D: a way to reconcile dissolution rates in the laboratory? Geochem. Cosmochim. Acta 273, 1–25.
Noiriel, C., Soulaine, C., 2021. Pore-scale imaging and modelling of reactive flow in evolving porous media: tracking the dynamics of the fluid–rock interface. Transport Porous Media 140 (1), 181–213.
Nooraiepour, M., Masoudi, M., Shokri, N., et al., 2021. Probabilistic nucleation and crystal growth in porous medium: new insights from calcium carbonate precipitation on primary and secondary substrates. ACS Omega 6 (42), 28072–28083.
Offeddu, F.G., Cama, J., Soler, J.M., et al., 2014. Direct nanoscale observations of the coupled dissolution of calcite and dolomite and the precipitation of gypsum. Beilstein J. Nanotechnol. 5 (1), 1245–1253.
Pan, Y., Li, Y., Ma, Q., et al., 2021. The role of Mg^{2+} in inhibiting $CaCO_3$ precipitation from seawater[J]. Mar. Chem. 237, 104036.
Peng, C., Crawshaw, J.P., Maitland, G.C., et al., 2015. Kinetics of calcite dissolution in CO_2-saturated water at temperatures between (323 and 373) K and pressures up to 13.8 MPa. Chem. Geol. 403, 74–85.
Pokrovsky, O., Golubev, S., Schott, J., et al., 2009. Calcite, dolomite and magnesite dissolution kinetics in aqueous solutions at acid to circumneutral pH, 25 to 150 °C and 1 to 55 atm pCO_2: new constraints on CO_2 sequestration in sedimentary basins. Chem. Geol. 265, 20–32.
Pilotti, M., Succi, S., Menduni, G., 2002. Energy dissipation and permeability in porous media. EPL 60 (1), 72.
Plummer, L.N., Wigley, T.M.L., Parkhurst, D.L., 1978. The kinetics of calcite dissolution in CO_2-water systems at 5 °C to 60 °C and 0.0 to 1.0 atm CO_2. Am. J. Sci. 278 (2), 179–216.
Qi, L., 2020. Characteristics and inspiration of ultra-deep fault-karst reservoir in the Shunbei area of the Tarim Basin, 01 China Petrol. Explor. 25, 102–111 (in Chinese).
Renard, F., Weiss, J., Mathiesen, J., et al., 2018. Critical evolution of damage toward system-size failure in crystalline rock. J. Geophys. Res. Solid Earth 123 (2), 1969–1986.
Ruiz-Agudo, E., Kudłacz, K., Putnis, C.V., et al., 2013. Dissolution and carbonation of portlandite [$Ca(OH)_2$] single crystals. Environ. Sci. Technol. 47 (19), 11342–11349.
Ruiz-Agudo, E., Putnis, C.V., Putnis, A., 2014. Coupled dissolution and precipitation at mineral–fluid interfaces. Chem. Geol. 383, 132–146.
Singurindy, O., Berkowitz, B., 2005. The role of fractures on coupled dissolution and precipitation patterns in carbonate rocks. Adv. Water Resour. 28 (5), 507–521.
Sjöberg, E.L., Rickard, D., 1983. The influence of experimental design on the rate of calcite dissolution. Geochem. Cosmochim. Acta 47 (12), 2281–2285.
Smith, M.M., Sholokhova, Y., Hao, Y., et al., 2013. CO_2-induced dissolution of low permeability carbonates. Part I: characterization and experiments. Adv. Water Resour. 62, 370–387.
Smith, M.M., Hao, Y., Mason, H.E., et al., 2014. Experiments and modeling of variably permeable carbonate reservoir samples in contact with CO_2-acidified brines. Energy Proc. 63, 3126–3137.
Smith, M.M., Dai, Z., Carroll, S.A., 2017. Illite dissolution kinetics from 100 to 280 °C and pH 3 to 9. Geochem. Cosmochim. Acta 209, 9–23.
Starchenko, V., Ladd, A.J.C., 2018. The development of wormholes in laboratory-scale fractures: perspectives from three-dimensional simulations. Water Resour. Res. 54 (10), 7946–7959.
Steefel, C.I., DePaolo, D.J., Lichtner, P.C., 2005. Reactive transport modeling: an essential tool and a new research approach for the Earth sciences. Earth Planet Sci. Lett. 240 (3–4), 539–558.
Steefel, C.I., Beckingham, L.E., Landrot, G., 2015. Micro-continuum approaches for modeling pore-scale geochemical processes. Rev. Mineral. Geochem. 80 (1), 217–246.
Steefel, C.I., MacQuarrie, K.T.B., 2018. Approaches to modeling of reactive transport in porous media. React. transport porous media 83–130.
Sun, W., Jayaraman, S., Chen, W., et al., 2015. Nucleation of metastable aragonite $CaCO_3$ in seawater[J]. Proc. Natl. Acad. Sci. USA 112 (11), 3199–3204.
Tartakovsky, A.M., Meakin, P., Scheibe, T.D., et al., 2007a. Simulations of reactive transport and precipitation with smoothed particle hydrodynamics. J. Comput. Phys. 222 (2), 654–672.
Tartakovsky, A.M., Meakin, P., Scheibe, T.D., et al., 2007b. A smoothed particle hydrodynamics model for reactive transport and mineral precipitation in porous and fractured porous media. Water Resour. Res. 43 (5).
Varzina, A., Cizer, Ö., Yu, L., et al., 2020. A new concept for pore-scale precipitation-dissolution modelling in a lattice Boltzmann framework–Application to portlandite carbonation. Appl. Geochem. 123, 104786.

Wang, Y., 2019. Multiple Originanl Mechanisms of the Ordovician Reservoir and Their Control on Hydrocarbon Charging in Shuntuoguole Area, Tarim Basin. China University of Geosciences (in Chinese).

Wang, T., Song, D., Li, M., et al., 2014. Natural gas source and deep gas exploration potential of the Ordovician Yingshan Formation in the Shunnan-Gucheng region, Tarim Basin. Oil Gas Geol. 35 (6), 753–762 (in Chinese).

Wellman, T.P., Grigg, R.B., McPherson, B.J., et al., 2003. Evaluation of CO_2-brine-reservoir Rock Interaction with Laboratory Flow Tests and Reactive Transport modeling[C]//International Symposium on Oilfield Chemistry. OnePetro.

Xu, R., Li, R., Ma, J., et al., 2017. Effect of mineral dissolution/precipitation and CO_2 exsolution on CO_2 transport in geological carbon storage. Acc. Chem. Res. 50 (9), 2056–2066.

Xu, T., Sonnenthal, E., Spycher, N., et al., 2006. TOUGHREACT—a simulation program for non-isothermal multiphase reactive geochemical transport in variably saturated geologic media: applications to geothermal injectivity and CO_2 geological sequestration. Comput. Geosci. 32 (2), 145–165.

Yang, L., Yu, L., Liu, K., et al., 2022a. Coupled effects of temperature and solution compositions on metasomatic dolomitization: significance and implication for the formation mechanism of carbonate reservoir. J. Hydrol. 604, 127199.

Yang, L., Zhu, G., Li, X., et al., 2022b. Influence of crystal nucleus and lattice defects on dolomite growth: geological implications for carbonate reservoirs. Chem. Geol. 587, 120631.

Zhang, Y., Jiang, F., Tsuji, T., 2022. Influence of pore space heterogeneity on mineral dissolution and permeability evolution investigated using lattice Boltzmann method. Chem. Eng. Sci. 247, 117048.